The Astrophysical Journal, 886:20 (14pp), 2019 November 20 https://doi.org/10.3847/1538-4357/ab488a

Bayesian Time-resolved Spectroscopy of GRB Pulses

Hoi-Fung Yu[1,2,3], Hüsne Dereli-Bégué[1,2,4], and Felix Ryde[1,2]
[1] Department of Physics, KTH Royal Institute of Technology, AlbaNova, SE-10691 Stockholm, Sweden; davidyu@hku.hk
[2] Oskar Klein Centre for Cosmoparticle Physics, AlbaNova, SE-10691 Stockholm, Sweden
[3] Faculty of Science, The University of Hong Kong, Pokfulam, Hong Kong
[4] Max Planck Institute for Extraterrestrial Physics, Giessenbachstrasse 1, D-85748 Garching, Germany
Received 2018 October 16; revised 2019 August 22; accepted 2019 September 23; published 2019 November 14

Abstract

We performed time-resolved spectroscopy on a sample of 38 single pulses from 37 gamma-ray bursts detected by the *Fermi*/Gamma-ray Burst Monitor during the first 9 yr of its mission. For the first time a fully Bayesian approach is applied. A total of 577 spectra are obtained and their properties studied using two empirical photon models, namely the cutoff power law (CPL) and Band model. We present the obtained parameter distributions, spectral evolution properties, and parameter relations. We also provide the result files containing this information for usage in further studies. It is found that the CPL model is the preferred model, based on the deviance information criterion and the fact that it consistently provides constrained posterior density maps. In contrast to previous works, the high-energy power-law index of the Band model, β, has in general a lower value for the single pulses in this work. In particular, we investigate the individual spectrum in each pulse, that has the largest value of the low-energy spectral indexes, α. For these 38 spectra, we find that 60% of the α values are larger than $-2/3$, and thus incompatible with synchrotron emission. Finally, we find that the parameter relations show a variety of behaviors. Most noteworthy is the fact that the relation between α and the energy flux is similar for most of the pulses, independent of any evolution of the other parameters.

Key words: catalogs – gamma-ray burst: general – methods: statistical

Supporting material: figure sets, machine-readable table

1. Introduction

The study of spectral shapes of the photon flux observed from astrophysical objects is a powerful tool to investigate the underlying physical processes. However, even after half a century of observations, the intrinsic spectral shape of the prompt emission of gamma-ray bursts (GRBs) remains unknown. Although during the past few decades many attempts have been made to fit the spectra with empirical, semiphysical, and physical photon models, we still have not found a comprehensive explanation of the emission mechanism of the prompt emission phase in GRBs. This is partly due to the large diversity in spectral shapes that is observed, which prevents a single and simple explanation to be found, and partly due to the inherent difficulties of performing gamma-ray spectroscopy.

Conventionally, mathematical functions (a.k.a. models) are fit to the observed photon counts. These are usually empirical models with the least possible number of parameters. Physical meaning of the parameters can be interpreted by comparing the values resulting from the fit to the predicted values from the theories. Among the frequently used models are the simple power law, cutoff power law (CPL), Band function (e.g., Band et al. 1993), smoothly broken power law, and the Planck function (a.k.a. the blackbody spectrum, e.g., Ghirlanda et al. 2003; Ryde 2004). Power laws are usually attributed to nonthermal processes, the Planck function indicates a thermal origin, and the Band function and broken power laws can be either thermal or nonthermal depending on the values of their parameters (i.e., the values of their spectral slopes).

Composite models have also been used to fit GRB spectra. For instance, González et al. (2003) first found that including a broader energy range beyond a few MeV, one burst observed by the Compton Gamma-Ray Observatory (CGRO) could be fitted by a power law, in addition to the Band function which dominates the emission at low energy. Moreover, Ryde (2005) fitted a Planck function plus a power law to CGRO/BATSE GRBs and found that the Planck component dominates. Similarly, using *Fermi* data, Abdo et al. (2009) fitted a Band function plus power law to GRB 090902B, while Ryde et al. (2010) fitted a multicolor blackbody instead of the Band component to the same burst. GRB 090902B is the most prominent example with the thermal Band or multicolor blackbody dominating over a nonthermal power law. The *Fermi*/GBM later confirmed the existence of an additional higher energy power-law component in a number of bursts (e.g., Ackermann et al. 2010; Guiriec et al. 2010). Furthermore, it was also shown that if a blackbody component is added to the nonthermal Band function the fit quality improves significantly in many cases (e.g., Guiriec et al. 2011, 2013; Axelsson et al. 2012; Burgess et al. 2014; Nappo et al. 2017). Later, Guiriec et al. (2015a) introduced a three-component model, which could be fitted to many bursts. Moreover, Vianello et al. (2018) reported detection of a high-energy break in two long GRBs (see also, Barat et al. 2000), and Oganesyan et al. (2018) reported an additional low-energy break in the spectrum of several GRBs.

In contrast to time-integrated spectroscopy (e.g., Goldstein et al. 2012; Gruber et al. 2014), i.e., the whole period of emission (or pulsation in the light curve) is treated as a single time bin, spectroscopy can also be done in a time-resolved manner (e.g., Yu et al. 2016), i.e., the light curve of the pulsation period is grouped into multiple time bins and spectral analysis is performed in each time bin individually. Indubitably, a burst often displays a varying behavior in its time-resolved emission. As an example of this, Guiriec et al. (2015b) found a pure blackbody at the beginning time of GRB

131014A, followed by mixed thermal and nonthermal components in later time, a property similarly demonstrated in other bursts as well (e.g., Ghirlanda et al. 2003; Ryde et al. 2011; Zhang et al. 2018). However, there is no single empirical model found to be preferred for every GRB spectrum.

GRB spectra were early noted to evolve significantly within each pulse (Golenetskii et al. 1983; Norris et al. 1986). Therefore, time-integrated spectra (as they are usually called) are actually averaged spectra, hence only time-resolved spectra should be used to directly infer physics. Alternatively, though, indirect methods can still be used as shown in Ryde & Svensson (1999). Several time-resolved spectral catalogs of GRBs exist in the literature (e.g., Kaneko et al. 2006; Yu et al. 2016), but they all make use of the frequentist approach. Similarly, spectra from overlapping pulses are likely to show averaged behaviors, so that separated pulses must be used in order to obtain the cleanest possible spectral results that are suitable to be used to draw physical conclusions. On the other hand, the temporal binning also affects the results of the spectral analysis. If the time bins are too coarse, there is spectral evolution within the bins; if the time bins are too fine, the signal-to-noise (or statistical significance) decreases. Therefore, the time bins must be defined in such a way that they capture the intrinsic variability of the light curve (i.e., they can be treated as "instantaneous") while maximizing the signal in each bin. The Bayesian block method (Scargle et al. 2013; Burgess 2014) that identifies statistically significant intensity changes in the light curve has been shown to be an adequate method for this task. This method results in time bins that only have a small, observed, intensity variation across their duration.

In the current study, we employ Bayesian inference which accounts for relevant prior information. During this process the background is incorporated into the model as a nuisance parameter which can be marginalized out. The resulting posterior probability distributions of parameters are obtained by the technique of Markov Chain Monte Carlo (MCMC). All parameter uncertainties are characterized by the highest posterior density credible intervals.

In this paper, we present the first systematic study of the time-resolved spectra of individual GRB pulses using the full Bayesian analysis method. Our sample is observed by the *Fermi*/Gamma-ray Burst Monitor (GBM) during its first 9 yr of mission and consists of 38 pulses from 37 bursts. The analysis methods and results are presented in Sections 2 and 3 respectively. We summarize and conclude our findings in Section 4. Unless otherwise stated, all error bars are given at the 68% (1σ) Bayesian credible level.

2. Methods and Results

2.1. Burst, Detector, and Pulse Selection

The *Fermi*/GBM has triggered on 2050 GRBs from 2008 July until 2017 March. The GBM consists of 14 detectors, of which 12 are sodium iodide (NaI, named from n0 to n9, na, and nb) detectors which cover roughly 8 keV to 1 MeV, and two are nondirectional bismuth germanium oxide (BGO, named b0 and b1) detectors which cover roughly 200 keV to 40 MeV (Bissaldi et al. 2009; Meegan et al. 2009). This arrangement makes the *Fermi*/GBM a powerful all-sky ($\gtrsim$8 sr that is not occulted by the Earth) surveying monitor with a wide energy range over 3 orders of magnitude. Preliminary GRB data is uploaded to the NASA/HEASARC database minutes after the trigger, including the trigger file and quick-look light curves. Detailed data files with the highest temporal (CTIME and TTE files) and spectral (CSPEC and TTE files) resolutions are downloaded from the spacecraft within hours. This makes the online *Fermi*/GBM GRB database a near real-time and most up-to-date GRB data repository.[5] For the spectral analysis described in Section 2.3, we used the standard *Fermi*/GBM analysis energy ranges: 8–30 keV and 40 keV to ~850 keV for the NaIs (avoiding the K-edge at 33.17 keV),[6] and ~250 keV to 40 MeV for the BGOs.

The purpose of our study is to follow the spectral evolution during individual emission episodes in the jet environment of the GRB. Therefore, we searched specifically for structures in the light curve that can be characterized as connected emission activities. We visually inspected all the 256, 512, and 1024 ms TTE (Time-Tagged Events) light curves and searched for such structures from all of the 2050 GRBs. We used those NaI detectors with viewing angles of less than 60° in order to maximize effective area (see Goldstein et al. 2012). In many of the selected cases, the emission episodes consist of individual pulses that are clearly separated by intervals of background level, which is identified as a flat or monotonic inter-pulse signal. However, since the shape of any connected emission activity from the jet is not, a priori, known (see, e.g., Lazzati et al. 2013), we want to avoid being too restrictive in our selection. Therefore, we also include in our sample emission episodes with additional features that can be interpreted as subpulses (that are more prominent than statistical fluctuation). However, these features should clearly be subdominant and be temporally connected with the main change in intensity. The variety of connected emission activities that were selected, for this step in defining the sample, are illustrated by the light curves shown in the figures in the Appendix. We note that another selection criterion to identify emission episodes could have been chosen, for instance, requiring a certain shape of the pulses, described by analytical functions (Norris et al. 1996; Hakkila & Giblin 2006). However, any such criteria are unnecessarily restrictive, since they assume a particular, analytical shape of the pulse, which we want to avoid. Finally, sometimes solar flares could also contribute to the low-energy channels which cause a broad pulse; however, these are easily identified by their emission characteristics. Such background events are identified and excluded in our study.

We selected 290 long bursts that were identified with at least one of these emission episodes, clearly separated by the nonemission background intervals. The next step in the selection process is to apply the method of Bayesian Blocks in order to identify spectra for which time-resolved spectroscopy can be performed. This step is the most restrictive and important and is therefore discussed in Section 2.3. The sample of 290 bursts is thus further reduced to 37 bursts, resulting in a sample of 577 spectra, which defines the final sample.

For the spectroscopy, we follow the procedure of the *Fermi*/GBM GRB time-integrated (Goldstein et al. 2012; Gruber et al. 2014) and time-resolved spectral catalogs (Yu et al. 2016) to select at most three NaIs and one BGO for the spectral analysis. The respective TTE and spectral response files are used for the sets of detectors selected. We followed the standard *Fermi*/GBM

[5] The data can be obtained by either visiting https://heasarc.gsfc.nasa.gov/W3Browse/fermi/fermigbrst.html or using the built-in command of `3ML` (Vianello et al. 2015).

[6] https://fermi.gsfc.nasa.gov/ssc/data/analysis/GBM_caveats.html

catalog analysis method to use the suitable response files. All the response files used in this study are automatically generated by the *Fermi*/GBM repository[7] according to the location obtained by the Burst Advocate (BA) from the GBM Team within weeks of the detection of the burst. The choice of the burst location and systematics that might affect the spectral analysis results are discussed in Connaughton et al. (2015).

2.2. Background Fitting

One of the NaI detectors that recorded the largest value photon counts per second is used to define the background intervals pre- and post-emission (i.e., the before and after the pulse). These intervals are then applied to all detectors. As a standard procedure in GRB background fitting of GBM data, we fit a polynomial, of order 0–4, to each energy channel (128 channels for TTE) of each of the detectors. The optimal order of the polynomial is determined by a likelihood ratio test independently for each energy channel. The polynomial is interpolated into the source and integrated over the source interval to obtain the background photon count flux. The error of the flux in each channel is also computed.

For some bursts, selection of two background intervals was not possible. For two cases in our sample (GRB 110817 and GRB 130305; Table 1), only one background interval was selected. This happens when the burst occurs right before the entrance of the South Atlantic Anomaly (SAA) region where the detectors must be shut down to avoid damage, or right after the exit of it. For one case (GRB 081009, see Table 1) there are several pulses separated by intervals that are background dominated. In order to better constrain the background polynomial shape, in this case, three background intervals were selected, instead.

2.3. Light-curve Binning and Spectral Fitting

The spectral analysis is done using the Bayesian spectral analysis package `3ML`[8] (Vianello et al. 2015). As a first step in time-resolved spectroscopy the light curves have to be rebinned into adequate intervals. Different methods can be used, for instance, binning by constant time interval dt, binning by statistical significance, and binning by Bayesian Blocks (Scargle et al. 2013). Burgess (2014) argued that in order to obtain the finest time bins (therefore the highest number of time bins) while minimizing the effect of mixed spectra caused by intrinsic spectral evolution (photons coming from distinct emission regions in the ejecta could arrive at the detector at the same time), the Bayesian Block method should be used. Therefore, for each burst, we rebinned the TTE light curve of the brightest NaI detector into Bayesian Blocks with a correct detection rate for a single change point of $p_0 = 0.01$ (see Equation (11) of Scargle et al. 2013). The Bayesian Block binning is then transferred and applied to all other detectors. We note, though, that the Bayesian Block method assumes that the variability in the light curve is the same over the whole energy range. However, the variability of the light curve might be dominated by the variability in the lowest energy photons, since GRB spectra are, in general, soft (e.g., Kaneko et al. 2006; Goldstein et al. 2012; Gruber et al. 2014; Yu et al. 2016, see also Section 3). Therefore, there is a possibility that spectral changes in the high-energy channels could be missed due to lower signal strength (Guiriec et al. 2015a). Moreover, we note that there is an implicit assumption that spectral variations are small when the variation in the light curve is small. This assumption is based on early studies, e.g., Golenetskii et al. (1983).

Since our aim is to study the time-resolved spectra of individual pulses, we need at least a few time bins in order to study the spectral evolution within the pulse. Yu et al. (2016) used a similar criterion that required the bursts to have at least five time bins with signal-to-noise ratio $\geqslant$30 (see Vianello 2018, for detailed derivation and discussion). The statistical significance, S, adopted in the current work is a test statistic that incorporates the information of signal-to-noise ratio and suitable for Poisson sources with Gaussian backgrounds (see Vianello 2018, for the definition of S). We found that the spectral parameters are typically well constrained for bins with statistical significance $S \geqslant 20$. Therefore, among the (initially selected) 290 bursts, we further require pulses to have at least five Bayesian Block time bins with $S \geqslant 20$ in order to study their time-resolved spectral evolution. This results in a sample of 38 single pulses in 37 bursts with at least five $S \geqslant 20$ time bins. This sample is listed in Table 1.

Nevertheless, for the purpose of a catalog, we still aim to present the properties of the selected sample with as few constraints as possible. Therefore, we present below the results of the overall statistics of this sample (without constraint on S)[9] as well as the statistics of this sample with $S \geqslant 20$. For the purpose of inferring physics from the spectral parameters, only bins with $S \geqslant 20$ should be used, which, for instance, is done in Ryde et al. (2019).

Several different models are typically used in the spectral analysis of GRBs, e.g., the CPL[10] and the Band function (BAND; Band et al. 1993). The GBM GRB time-resolved catalog (Yu et al. 2016) showed that CPL is preferred over the other frequently used models for a majority (70%) of bursts, according to the Castor C-Statistic (CSTAT; a modified version of the original Cash statistic derived by Cash 1979). Therefore, for the main analysis below, we fit CPL to all time bins of our 38 pulses. In addition, we also fit BAND to all pulses to allow for a comparison to be made between the models. For each time bin, a Poisson distribution for the source and a Gaussian distribution for the background is used to obtain the likelihood function. This is because the background is estimated from a polynomial fit and the source is not.

We inspected all posteriors of the spectra (2 empirical models for 577 spectra, making up a total of 1154 corner plots) and checked that `3ML` signals the fit has converged. We also double-checked that the four independent chains used in the MCMC sampling converged to the same maximum.

In Table 1, we list the 38 single pulses from 37 bursts that satisfy all these criteria (Column 1), together with the detectors used (Column 2), the source and background intervals (Columns 3–6), the total number of time bins (Column 7), and the number of time bins with minimum significance of 20 (Column 8), and the type of relations for parameter pairs α–$E_{\rm p}$, F–$E_{\rm p}$, and F–α (Columns 9–11), where α is the low-energy power-law index, $E_{\rm p}$ is the spectral peak, and F is the energy flux. The type of spectral evolution for each pulse is listed in Column 12. In addition, the Spearman's rank coefficient, r, for

[7] https://heasarc.gsfc.nasa.gov/W3Browse/fermi/fermigbrst.html
[8] https://threeml.readthedocs.io/en/latest/notebooks/Bayesian_tutorial.html
[9] Note, however, that the relevance of the data points is still provided by the size of the error bar.
[10] This model is also known as the Comptonized model, abbreviated as COMP due to its theoretical relation to the Comptonized spectral shape.

Table 1

GRB Name (Column 1), Together with the Detectors (Column 2), and the Source (Column 3) and Background Intervals (Columns 4–6) Used in the Analysis

GRB	Detectors	$\Delta T_{\rm src}$ (s)	$\Delta T_{\rm bkg,1}$ (s)	$\Delta T_{\rm bkg,2}$ (s)	$\Delta T_{\rm bkg,3}$ (s)	N	$N_{S\geqslant 20}$	α–$E_{\rm p}$ Type(r)	F–$E_{\rm p}$ Type(r)	F–α Type(r)	Spectral Evolution
(1)	(2)	(3)	(4)	(5)	(6)	(7)	(8)	(9)	(10)	(11)	(12)
081009140	(n3)b1	0. to 10.	−25. to −5.	15. to 30.	60. to 80.	19	16	−(0.12)	2(0.64)	1(0.60)	i.t.
081009140	(n3)b1	33. to 55.	−25. to −5.	15. to 30.	60. to 80.	13	6	−(0.77)	3(−0.43)	2(0.05)	h.t.s.
081125496	(na)nbb1	−5. to 20.	−20. to −10.	30. to 50.	…	12	6	1(−0.69)	1(−0.19)	1(0.74)	h.t.s.
081224887	n6n7(n9)b1	0. to 25.	−25. to −5.	30. to 60.	…	10	7	1(0.83)	1(0.83)	1(0.97)	h.t.s.
090530760	(n1)n2n5b0	−1. to 180.	−25. to −10.	200. to 250.	…	10	6	1(0.76)	1(0.95)	1(0.90)	h.t.s.
090620400	(n6)n7nbb1	−1. to 25.	−25. to −10.	30. to 45.	…	11	5	2(−0.02)	2(0.17)	1(0.48)	i.t.
090626189	(n0)n1b0	30. to 39.	−25. to −10.	80. to 95.	…	15	8	3(−0.12)	1(0.15)	1(0.84)	i.t.
090719063	n7(n8)b1	−1. to 25.	−25. to −10.	35. to 50.	…	15	11	2(0.65)	1(0.71)	1(0.83)	h.t.s. to i.t.
090804940	n3n4(n5)b0	−1. to 15.	−25. to −10.	25. to 40.	…	14	8	3(−0.15)	2(0.9)	3(−0.22)	i.t.
090820027	(n2)n5b0	25. to 60.	−20. to 10.	80. to 95.	…	25	19	2(0.53)	1(0.67)	1(0.79)	flat to i.t.
100122616	(n6)nab1	−5. to 40.	−20. to −10.	50. to 80.	…	14	5	2(−0.69)	2(−0.83)	1(0.78)	i.t. to ?
100528075	n6(n7)nbb1	−5. to 60.	−30. to −10.	66. to 100.	…	16	7	3(−0.44)	3(−0.17)	1(0.72)	h.t.s.
100612726	n3n4(n8)b0	−2. to 20.	−30. to −5.	25. to 100.	…	12	6	1(0.05)	1(0.03)	1(0.92)	h.t.s.
100707032	n7(n8)b1	0. to 30.	−20. to −5.	40. to 100.	…	19	13	1(0.58)	1(0.57)	1(0.97)	h.t.s.
101126198	(n7)n8nbb1	−5. to 40.	−30. to −15.	50. to 80.	…	15	7	1(−0.15)	2(0.38)	1(0.54)	flat to h.t.s.
110721200	(n6)n7n9b1	−1. to 20.	−25. to −10.	35. to 50.	…	12	9	1(0.22)	1(0.35)	2(0.51)	h.t.s. to s.t.h.
110817191	n6n7(n9)b1	−1. to 11.	−20. to −7.	…	…	9	5	1(0.21)	1(0.26)	1(0.98)	h.t.s.
110920546	(n0)n1n3b0	−1. to 160.	−15. to −5.	175. to 200.	…	14	10	2(−0.86)	1(0.88)	1(−0.71)	h.t.s.
111017657	(n6)n7n9b1	−5. to 20.	−25. to −10.	35. to 50.	…	13	6	1(−0.10)	1(−0.25)	1(0.92)	h.t.s. to s.t.h.
120919309	(n1)n2n5b0	−2. to 35.	−25. to −5.	60. to 100.	…	15	6	1(0.48)	1(0.55)	1(0.88)	i.t.
130305486	n6(n9)nab1	−3. to 35.	50. to 70.	…	…	13	8	2(−0.82)	2(−0.44)	1(0.81)	h.t.s. to flat
130612456	n6(n7)n8b1	−1. to 15.	−25. to −10.	25. to 45.	…	11	6	3(0.11)	2(0.54)	1(0.86)	flat
130614997	(n0)n1n3b0	−1. to 9.	−25. to −10.	20. to 45.	…	8	5	3(−0.20)	2(0.40)	1(0.60)	h.t.s.
130815660	(n3)n4n5b0	−1. to 47.	−25. to −10.	55. to 75.	…	13	5	1(−0.27)	1(−0.38)	1(0.93)	h.t.s.
140508128	(na)b1	−1. to 15.	−40. to −10.	100. to 150.	…	18	11	3(0.28)	2(0.47)	1(0.91)	i.t.
141028455	(n6)n7n9b1	0. to 40.	−30. to −10.	50. to 100.	…	18	12	2(0.63)	1(0.37)	1(0.85)	h.t.s.
141205763	(n2)n5b0	−2. to 20.	−40. to −10.	25. to 80.	…	14	5	1(0.46)	2(0.75)	1(0.75)	i.t.
150213001	n6n7(n8)b1	−1. to 10.	−25. to −10.	20. to 45.	…	24	19	1(0.03)	1(0.21)	1(0.46)	h.t.s. to i.t.
150306993	(n4)b0	−1. to 25.	−25. to −10.	35. to 55.	…	11	7	2(0.93)	2(0.83)	1(0.83)	h.t.s.
150314205	n1(n9)b1	−1. to 18.	−25. to −10.	30. to 55.	…	20	14	1(−0.23)	1(−0.36)	1(0.85)	h.t.s. to s.t.h.
150510139	n0n1(n5)b0	0. to 50.	−25. to −10.	65. to 95.	…	30	16	3(0.13)	1(0.13)	1(0.81)	s.t.h. to h.t.s.
150902733	(n0)n1n3b0	−1. to 25.	−25. to −10.	30. to 55.	…	22	14	1(0.13)	1(0.28)	1(0.85)	h.t.s. to i.t. to h.t.s.
151021791	n9(na)b1	−1. to 10.	−25. to −10.	25. to 45.	…	10	5	2(0.86)	1(0.75)	1(0.64)	h.t.s.
160215773	n3n4(n5)b0	160. to 200.	100. to 150.	250. to 300.	…	19	11	2(−0.60)	2(0.84)	1(−0.54)	i.t.
160530667	n1(n2)n5b0	−2. to 25.	−40. to −10.	40. to 80.	…	22	19	2(0.73)	1(0.84)	1(0.87)	s.t.h. to h.t.s.
160910722	n1n2(n5)b0	7. to 20.	−40. to −10.	40. to 80.	…	15	14	1(0.36)	1(0.15)	2(0.86)	h.t.s.
161004964	n3(n4)b0	−2. to 25.	−40. to −10.	40. to 80.	…	11	5	1(0.20)	2(0.02)	1(0.85)	h.t.s.
170114917	n1(n2)nab0	−1. to 20.	−25. to −10.	35. to 65.	…	15	9	2(−0.34)	1(−0.17)	1(0.87)	h.t.s. to ?

Note. The number of time bins using Bayesian blocks across the source interval (Column 7), and the number of time bins with statistical significance of at least 20 (Column 8) are also listed. Columns 9–11 list the type of parameter relations, with the Spearman's rank coefficient, r, in the brackets. Column 12 lists the evolutionary trend of the peak energy. The detector in brackets is the brightest one, used for background and Bayesian block fitting.

the parameter relations is also listed in the brackets of Columns 9–11 next to the type.

Finally, we note that the models used here are empirical in nature. Physical models can be used and directly compared to each other, but this is out of the scope of the current paper. Note also that model selection is based on prior experience and the statistics (frequentist or Bayesian) cannot identify the true model but only can compare competing ones. While the current study focuses on extracting the parameters of the best model from previous experience, a more standardized study on all kinds of empirical and physical models should be done in the future.

3. Spectral Results

The complete fitting results for the CPL and BAND models of all 577 spectra are listed in the table of Appendix C. For each pulse, we list the start and stop times of the Bayesian blocks (Columns 1 and 2), the significance S (Column 3), the CPL fitted parameters (normalization K (ph s^{-1} cm^{-2} keV^{-1}), the low-energy power-law index α, the cutoff energy E_c, (keV, Columns 4–6), the derived CPL peak energy E_p (keV, Column 7), the CPL energy flux, F (erg s^{-1} cm^{-2}, Column 8), the BAND fitted parameters (normalization $K_{\rm BAND}$, ph s^{-1} cm^{-2} keV^{-1}), the low-energy power-law index $\alpha_{\rm BAND}$, the high-energy power-law index $\beta_{\rm BAND}$, the peak energy $E_{\rm p,\ BAND}$ (keV, Columns 9–12), the BAND energy flux, $F_{\rm BAND}$ (erg s^{-1} cm^{-2}), the difference in the deviance information criterion (DIC) between CPL and BAND, $\Delta{\rm DIC} = {\rm DIC_{BAND}}-{\rm DIC_{CPL}}$ (Column 14), and the effective number of parameters of CPL and BAND, $p_{\rm DIC}$ and $p_{\rm DIC,BAND}$ (Columns 15 and 16).

We also provide the analysis result files in `FITS` format for every time bin, which are available at 10.5281/zenodo.2601901. They provide complete information of the fits such as the parameter values, covariance matrices, and the statistical information criteria. They can be read readily by `3ML` to plot the resulting spectra and the posterior probability distributions. The results can be used for further studies of the spectra of these pulses.

3.1. CPL versus BAND: which One Is "Better"?

We have fitted the data with the empirical models which have been used as standard models in the field and which have been shown to be compatible with the data (e.g., Kaneko et al. 2006; Goldstein et al. 2012; Gruber et al. 2014; Yu et al. 2016). In these catalogs, the empirical model fits have also been compared to each other, using the difference in CSTAT. Similarly, in Bayesian statistics, model comparison is done using the so-called information criteria. However, the "best" information criterion to use is an active research topic in Bayesian statistics (see, e.g., Gelman et al. 2014, for a recent discussion). In this paper, we compare models by adopting the DIC (Spiegelhalter et al. 2002), defined as ${\rm DIC} = -2\log[p({\rm data}|\hat{\theta})] + 2p_{\rm DIC}$, where $\hat{\theta}$ is the posterior mean of the parameters and $p_{\rm DIC}$ is a term to penalize the more complex model for overfitting (see, Section 3.3 of Gelman et al. 2014).[11]

[11] The $p_{\rm DIC}$ approaches the total number of parameters of the model when the posterior mean and mode are similar. However, when the posterior is highly skewed, it can become negative. We found that negative $p_{\rm DIC}$ are associated with time bins having low signal-to-noise ratio. In such cases, the value of DIC indeed cannot determine whether a model is preferred. In the extreme example where low signal is present, all models will perform equally "bad," and in this case the values of DIC are not trustable.

The values of the difference between BAND's and CPL's DIC, defined as $\Delta{\rm DIC} = {\rm DIC_{BAND}}-{\rm DIC_{CPL}}$, are listed in Column 14 of the table in Appendix C. Since DIC is defined as the negative logarithm of the probability of predicting the observed data given the posterior mean, a positive value of ΔDIC would mean that the CPL is preferred given the observed data (as seen in Column 14).

However, just like any other statistical measures, attempting to summarize the multidimensional posterior distribution in just one number can often be misleading. In some cases, we see that $|\Delta{\rm DIC}|$ can be as large as hundreds of thousands. It is of course very dangerous to blindly believe such a number and claim that one model is exceedingly better than the other. Thus, we need to check the values of $p_{\rm DIC}$ for both models (Columns 15 and 16). We checked that in almost all of the cases for which the ΔDIC is highly negative, so is $p_{\rm DIC,BAND}$. We found that when ${\rm DIC_{BAND}} < {\rm DIC_{CPL}}$, $p_{\rm DIC,BAND} \ll 0$ in most cases.

The posterior corner plot contains the two-dimensional probability density maps for each pair of parameters. The marginal probability for each parameter is also computed by the integral of the conditional probability over all but the desired parameter. An acceptable fit is indicated when the probability density map is centered within the prior limits. When the probability density of the normalization increases toward zero, upper limits can only be inferred. A check to the posteriors of those Band fits with highly negative $p_{\rm DIC,BAND}$ reveals that the normalization is often small, indicating that the addition of an extra power-law segment has a negative impact on the fit.

In this study, we use the same empirical model throughout the whole burst for consistency. However, when there is enough data in the high-energy range (higher than a few 100 keV where the spectral peak usually resides), the Band function might be preferred as indicated by the value of ΔDIC. This usually occurs around the peak time in the light curve. Although the models used in the current study are empirical, they are useful in extracting spectral parameters and their evolution, which can give an indication of the physical model underlying the emission. Such investigations can thus motivate physical models to be fit directly to the data.

In summary, we found that the cutoff power-law model is the preferred model, since it systematically has a lower DIC value. In addition, the resulting parameters for the CPL fits are constrained within the prior ranges more often than for the Band function fits. This result is consistent with previous GBM spectral catalogs. However, we note that the preference of the exponential cutoff model could be due to the lack of photon counts at high energy in the GBM energy channels.

3.2. Parameter Distributions

Figures 1 and 2 show the overall parameter distributions, including α, E_c, and β, E_p and the derived parameters, E_p (for CPL) and F. The average values and standard deviations of the distributions are listed in Table 2.

Since the errors of the fitted spectral parameters could not be taken into consideration in the histograms, we performed kernel density estimation (KDE) on individual parameter distributions. A Gaussian kernel is chosen. In order to be conservative, the standard deviation of the Gaussian kernel is set equal to the larger of the asymmetrical errors. The KDEs are overlaid on Figures 1 and 2.

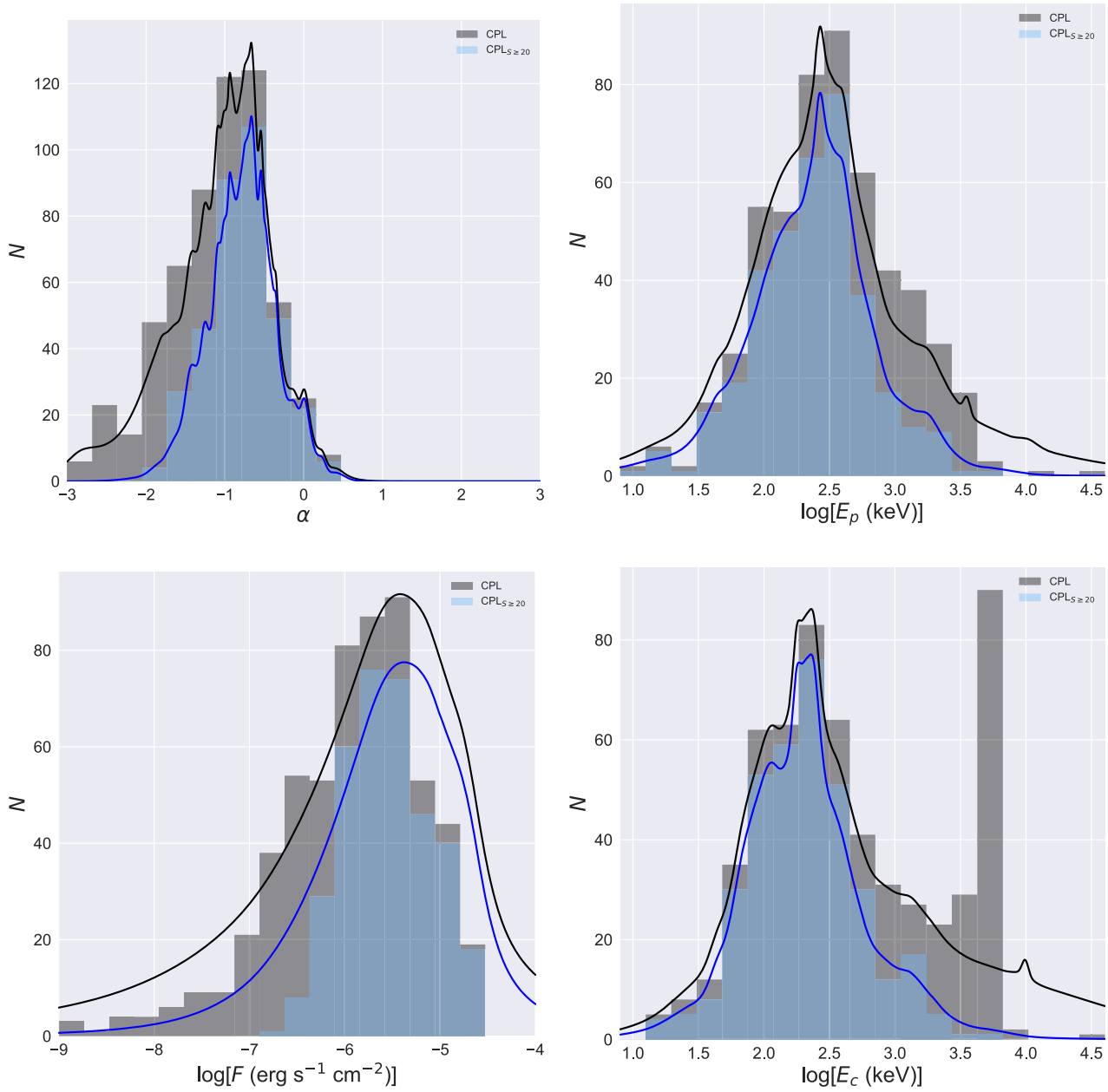

Figure 1. Parameter distributions of the fitted parameters of CPL. Black histogram shows the distributions regardless of significance, and blue histogram shows the distributions with $S \geqslant 20$. The curves represent the kernel density estimation (KDE) of the distributions, using Gaussian kernels where the standard deviation is set to the larger one of the asymmetrical errors. For $E_{\rm p}$ and $E_{\rm c}$, only the values within the GBM energy range (8 keV–40 MeV) are shown.

The average values of α, $E_{\rm p}$, and F distributions for CPL and BAND agree within 1σ for $S \geqslant 20$. Since the data and analysis conditions of the current study are different from previous catalogs (e.g., Gruber et al. 2014; Yu et al. 2016), the parameter distributions shown here should not be treated as a one-to-one direct comparison. Nevertheless, we still find that the distributions of α and $E_{\rm p}$ are in agreement with previous time-resolved catalogs (e.g., see Table 2 and Figure 3 of Yu et al. 2016). Therefore, the frequentist and Bayesian analysis give consistent results. The distribution of β that we obtained has lower values than that of Yu et al. (2016), who did not distinguish between single and composite pulses (see the lower right panel of Figure 3 therein). This indicates that single pulses are in general softer, and that the higher values of β might be a result of overlapping spectra from composite pulses which contain photons from various emission sites and times.

It is observed that the majority of the low-significance data points in the α–$E_{\rm c}$ plot have $\alpha < -2$ and $E_{\rm c} \sim 5$ MeV, which is reflected by an unexpected peak at 5 MeV in the $E_{\rm c}$ histogram. First, we noticed that when plotting the $E_{\rm c}$ distribution of time bins with $S \geqslant 20$ only, the peak at 5 MeV completely disappears. Second, these are spectra not from one particular burst but from either the beginning or the end of multiple bursts. Third, we also noticed that noise dominates at energies $\gtrsim$1 MeV, resulting in overall lower significance for the time bin. Last but not least, this peak does not show up in the KDE. This implies the errors on those values of $E_{\rm c}$ are very large, which means that the Bayesian

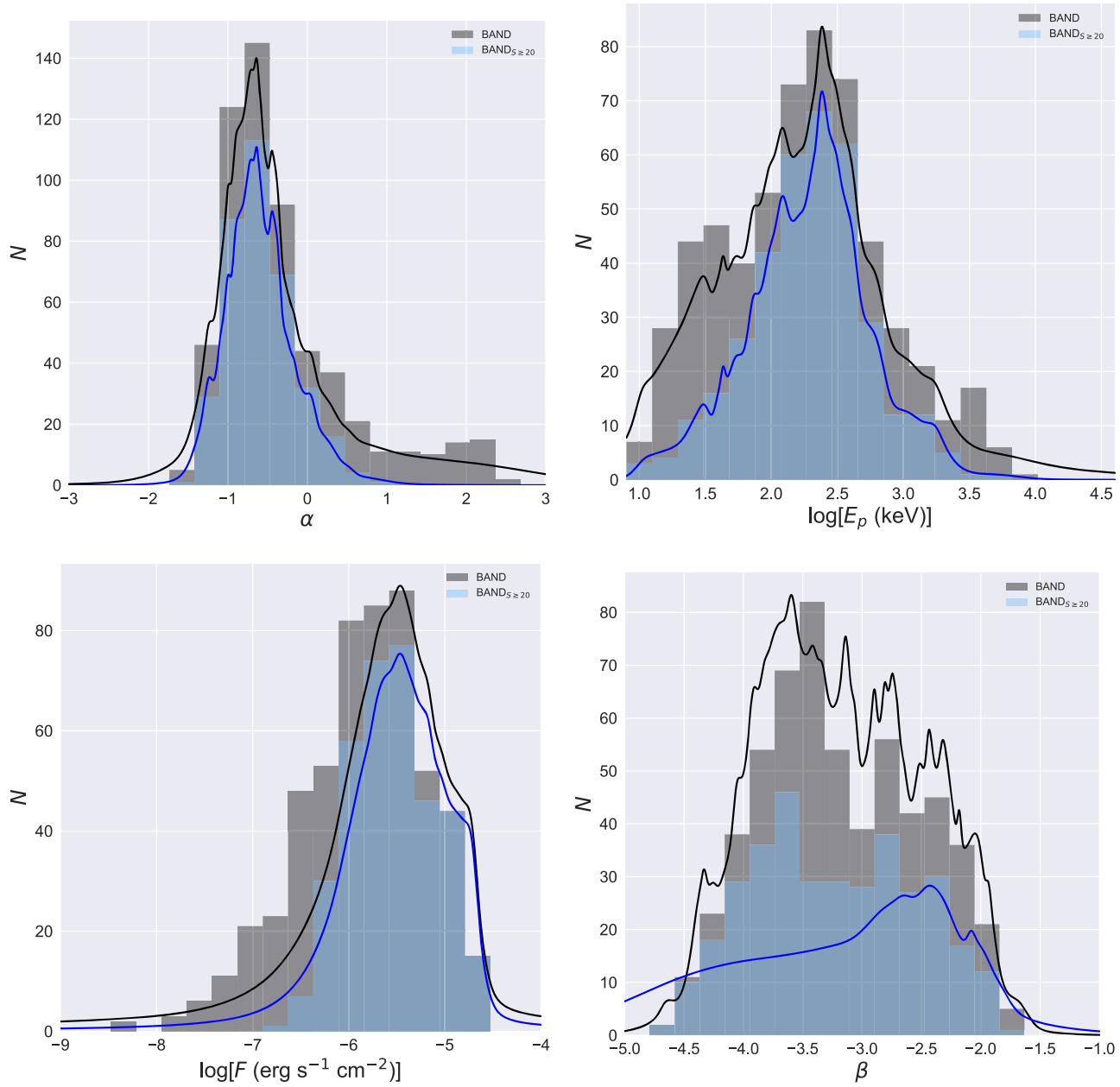

Figure 2. Parameter distributions of the fitted parameters of BAND. Black histogram shows the distributions regardless of significance, and blue histogram shows the distributions with $S \geqslant 20$. The curves represent the kernel density estimation (KDE) of the distributions, using Gaussian kernels where the standard deviation is set to the larger one of the asymmetrical errors. For $E_{\rm p}$ only the values within the GBM energy range (8 keV–40 MeV) are shown.

inference struggled to find a cutoff point. We therefore repeated the spectral analysis on these time bins using a simple power law, and found that they are indeed well fit by a single power law. Since noise dominates at energy $E \gtrsim 1$ MeV for these spectra, the value of $E_{\rm c}$ cannot go beyond 5 MeV and is highly uncertain as indicated by the error bars. This indicates that for low-significance time bins, the spectrum can be sufficiently described by a single power law and a spectral break is not necessary.

In Figures 1 and 2, the α-distributions contain all analyzed time bins. A consequence of this is that individual bursts contribute to the distribution with a varying number of bins. This leads to a bias toward bursts with many time bins. In order to avoid such a bias, one can instead interpret the distribution containing only one bin per burst. Furthermore, the best bin to characterize the emission mechanism during a pulse is the bin containing the largest value of α indexes in each pulse/burst. The reason for this is that physical models typically have a limit to how hard the spectra are allowed to get. Therefore, if one single bin violates such a limit the corresponding emission model is rejected by the data. This is, of course, under the assumption that a single emission mechanism is responsible for the full duration. We, therefore, identify the largest value of α in each of the 38 pulses in the sample: $\alpha_{\rm max} \equiv \max(\alpha(t))$. We present their histogram in Figure 3 in which we also plot the $\alpha = -2/3$-line, which is the "line of death" for synchrotron emission. In order to calculate the fraction of $\alpha_{\rm max}$-values that are incompatible with synchrotron emission, i.e., the fraction of bins lying to the right side of the red line, we identify the cases for which the 1σ lower limit of the $\alpha_{\rm max}$ is larger than $-2/3$.

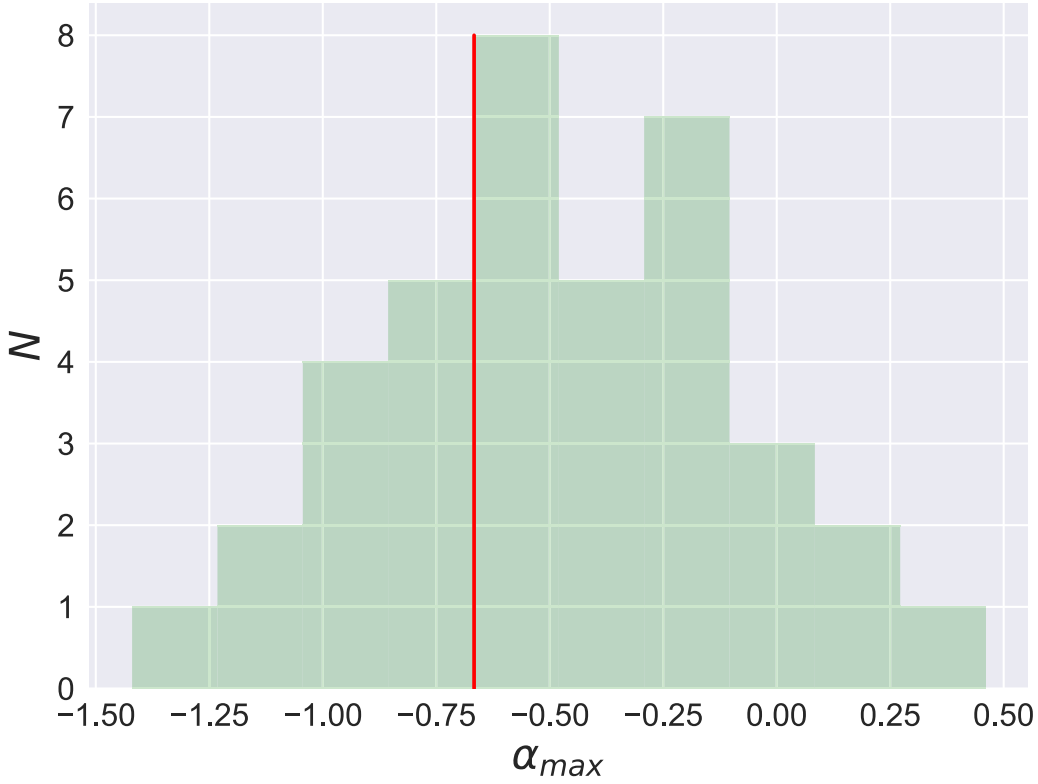

Figure 3. Histogram of the maximal value of α in each of the 38 pulses in the sample. The red line indicated the line of death for the synchrotron interpretation for individual pulses, assuming that the same emission mechanism operates throughout the pulse. 60% of the pulses have $\alpha_{\rm max}$ (within a 1σ lower limit of the error) that is incompatible with synchrotron emission.

Table 2
The Values of the Average and Standard Deviation of the Parameter Distributions

Model	α	$\log_{10}(E_{\rm p}/{\rm keV})$	$\log_{10}(F/10^{-6}\ {\rm erg^{-1}\ s^{-1}\ cm^{-2}})$	$\log_{10}(E_{\rm c}/{\rm keV})$	β
CPL	-1.07 ± 0.63	$\log_{10}(331) \pm 0.53$	$\log_{10}(1.17) \pm 0.77$	$\log_{10}(457) \pm 0.68$	…
$\rm CPL_{S\geqslant 20}$	-0.79 ± 0.43	$\log_{10}(234) \pm 0.44$	$\log_{10}(2.86) \pm 0.44$	$\log_{10}(206) \pm 0.42$	…
BAND	-0.31 ± 0.84	$\log_{10}(170) \pm 0.60$	$\log_{10}(1.39) \pm 0.68$	…	-3.18 ± 0.66
$\rm BAND_{S\geqslant 20}$	-0.59 ± 0.41	$\log_{10}(193) \pm 0.44$	$\log_{10}(2.90) \pm 0.43$	…	-3.23 ± 0.68

Note. For $E_{\rm p}$ and $E_{\rm c}$, only values within the GBM energy range (8 keV–40 MeV) are used in the calculation.

We find that a majority of the pulses (60 %) are inconsistent with synchrotron emission, using this criterion. This fraction is significantly larger than what is found by applying the line of death to the full distribution of α-values (Preece et al. 1998, see also Ghirlanda et al. 2002).

3.3. Spectral Evolution

In Appendix A, we show the CPL and BAND parameter evolutions across the duration of each pulse, with color scale from light blue (start) to deep blue (end) showing temporal evolution and the light curve overlaid. Data points with red, orange, yellow, and no circles indicate statistical significance $S \geqslant 20$, $20 > S \geqslant 15$, $15 > S \geqslant 10$, and $S < 10$, respectively. Many of the low-significance data points are not constrained, as seen from the huge negative-side error bars.

It is observed that the values of the low-energy spectral indices of CPL and BAND, α and $\alpha_{\rm BAND}$, are approximately equal to within errors and track each other during the main emission periods of the pulses (which are also the most significant time bins, indicated by red circles). As discussed in Section 3.2, $\alpha_{\rm BAND}$ tends to have slightly higher values than α, and $\beta_{\rm BAND}$ usually have lower values than -3.

In most pulses the evolution of α exhibits a variation that appears to track the variation in the light curve. This is most pronounced around the pulse peak, where the time bins also have the highest significance. In some cases there is a slight temporal shift between the α-variation and the light curve. These observed properties are similar to earlier findings by, for instance, Crider et al. (1997), Ghirlanda et al. (2002), Lloyd-Ronning & Petrosian (2002), and Basak & Rao (2014) and are further discussed in Section 3.5.3.

For the behavior of the peak energy, it is obvious that in almost all time bins $E_{\rm p}$ and $E_{\rm p,BAND}$ are well within half an order of magnitude. It is noticed that $E_{\rm p,BAND} \lesssim E_{\rm p}$ during time bins with $S \geqslant 20$. Combining with the observation that $\alpha_{\rm BAND} > \alpha > \beta_{\rm BAND}$, this suggests that BAND is trying to fit the spectrum by mimicking the curvature below the CPL's

peak energy using two power-law segments. This can also explain the hard BAND spectrum during low-significance time bins: the overshot of $\beta_{\rm BAND}$ at high energies is tolerated by the noisy time bins.

The evolution of $E_{\rm p}$ is observed to exhibit various trends (Column 11 of Table 1). We found that 16 exhibit pure hard-to-soft (h.t.s.) evolution (42%), while 8 exhibit pure intensity tracking (i.t.) evolution (21%). Seven pulses change from either h.t.s. or flat to i.t. or soft-to-hard (s.t.h.) evolution. Lu et al. (2012) studied simulated GRB pulses and claimed that an i.t. evolving pulse can be composed by multiple h.t.s. evolving pulses. Four cases cannot be classified into the above categories: GRB 150510139 and GRB 160530667 exhibit s.t.h. to h.t.s. evolution; GRB 100122616 i.t. to unclassified, and GRB 170114917 h.t.s. to unclassified (marked by a "?") during part of the pulse.

The calculated energy fluxes for CPL and BAND, F and $F_{\rm BAND}$, agree very well for every spectrum and they basically track the photon light curve. During low-significance time bins, $F_{\rm BAND}$ is always larger than F, which could be explained by the aforementioned harder BAND spectrum.

3.4. Global Parameter Relations

Figure 4 shows the overall parameter relations within the GBM energy range (8 keV–40 MeV) with statistical significance $S \geqslant 20$, in five panels of the parameter pairs: α–$E_{\rm c}$ for CPL (upper left panel), α–$E_{\rm p}$ for CPL and BAND (upper right), F–$E_{\rm p}$ for CPL and BAND (middle left), F–α for CPL and BAND (middle right), and β–α for BAND (bottom). It is observed that the distributions of parameters for CPL and BAND show no obvious difference nor any global relation.

For statistical significance $S \geqslant 20$, all except one α-values are between -2 and 1 to within 1σ uncertainty for both CPL and BAND, which are typically observed in studies of GRB prompt spectra. We note that that β can be very negative (~ -3 or below). There are two possible reasons for this. Either the BAND model is trying to mimic a cutoff in the high-energy spectrum, or the poor count statistics at high energies prevents a determination of β (see, e.g., Kaneko et al. 2006; Goldstein et al. 2012; Gruber et al. 2014; Yu et al. 2016). The threshold of F for the high-significance data points is $\sim 10^{-7}$–10^{-6} erg s^{-1} cm^{-2}.

The peak energy, $E_{\rm p}$, for BAND is a fitted parameter, while that for CPL is calculated from $E_{\rm p} = (\alpha + 2)E_{\rm c}$. Notice that when α has lower values than -2 or when $\beta_{\rm BAND}$ has higher values than -2, $E_{\rm p}$ becomes negative and thus there is no peak in the νF_ν spectrum.

3.5. Individual Parameter Relations

Relations over individual pulses are of greatest interest since they carry the information closest to the physics of the emission. We, therefore, provide the relation plots of the 38 pulses in our sample in Appendix B. In the figures, the relation between α and $E_{\rm p}$ are shown in the left-hand panels; the relation between energy flux F and $E_{\rm p}$, i.e., the Golenetskii correlation (Golenetskii et al. 1983), are shown in the middle panels; and, finally, the relation between F and α are shown in the right-hand panels.

Below, we will discuss the appearances of the temporal tracks in the relation planes by visual inspection. We consider all time bins with significance $S > 10$ (i.e., yellow, orange, and red data points) that are fitted with a CPL function.

3.5.1. α–E_p Relation

The α–$E_{\rm p}$ relations show three main types of behaviors. The most common behavior is a nonmonotonic relation, with a clear break. This occurs in 17 pulses. The break either occurs at the maximal α-value (e.g., GRB 081125), or at the minimum $E_{\rm p}$ (e.g., GRB 150314). Another common behavior (12 pulses) is a monotonic, straight line in the linear-log plots (see, also Crider et al. 1997). Of these bursts, 6 have a positive relation (e.g., GRB 090719) and 6 have a negative relation (e.g., GRB 130305), even if GRB 090620 has a weaker correlation. The third behavior (7 bursts) is given by pulses in which the $E_{\rm p}$ does not vary much, while α does vary more significantly. This leads to a vertical relation, or a weakly negative relation (e.g., GRB 100528). In one of these cases (GRB 090804), though, there is only little variation in α as well, it even being consistent with a constant at around $\alpha \sim -0.5$. In Table 1, all bursts are assigned to one of these three groups, 1, 2, and 3, respectively. The remaining two pulses (both in GRB 081009) do not show any clear trend. For the second pulse in GRB 081009, the reason is that in most of the high-significance time bins there is no $E_{\rm p}$ (the νF_ν spectrum is monotonically decreasing) leaving only a few data points for the relation.

To quantify the relations, we calculate the Spearman's rank coefficient, r, which is also provided in Table 1. In general, values over 0.7 indicate strong correlations. However, only for a few pulses (8 cases) $r > 0.7$. A large majority of the pulses (20 cases) have weak correlations as indicated by the r-value being below 0.4.

It is noteworthy that among all the $E_{\rm p}$–α-relations, only three pulses have a relation that follows what is expected for synchrotron emission (Lloyd & Petrosian 2000, their Figure 5), namely GRB 120919, GRB 130815, and GRB 141205, see further discussion in Ryde et al. (2019).

3.5.2. F–E_p Relation

Turning over to the Golenetskii relation, again three main different types of relations are revealed (see, also Borgonovo & Ryde 2001; Firmani et al. 2009; Ghirlanda et al. 2010). The most common behavior (in 23 pulses) is a nonmonotonic relation with a distinct break and having power-law segments (e.g., GRB 160530). The break typically occurs at the flux peak of the pulse, that is, the relation is different during the rise phase and the decay phase of the pulse. Another common behavior has a relation described by a single power law (in 13 of the pulses). Of these, 11 pulses have a positive relation (e.g., GRB 090804) and in 2 cases it is negative (e.g., GRB 130305). Finally, in two cases there are no clear trends. These pulses are from the second episode of GRB 081009 (again mainly due to fact that many of the $E_{\rm p}$ are not determined) and from GRB 100528. In Table 1, these three groups, are denoted by 1, 2, and 3, respectively.

For these relations, we also calculate the Spearman's rank coefficient (provided Table 1). Again, only a few pulses (11 cases) have strong correlations ($r > 0.7$), while a large majority of the pulses (18 cases) have weak correlations ($r < 0.4$).

GRB 090804 is an interesting case in which the Golenetskii relation is prominent, but both $E_{\rm p}$–α and the F–α relations are very weak. Such a behavior is, however, an exception. We also note that Guiriec et al. (2013, 2015a, 2015b, 2016a, 2016b) have shown that, in their three-component model, a correlation between the energy flux and the νF_ν peak energy manifests itself, for one of the nonthermal components, even in GRBs where the Golenetskii relation is not valid.

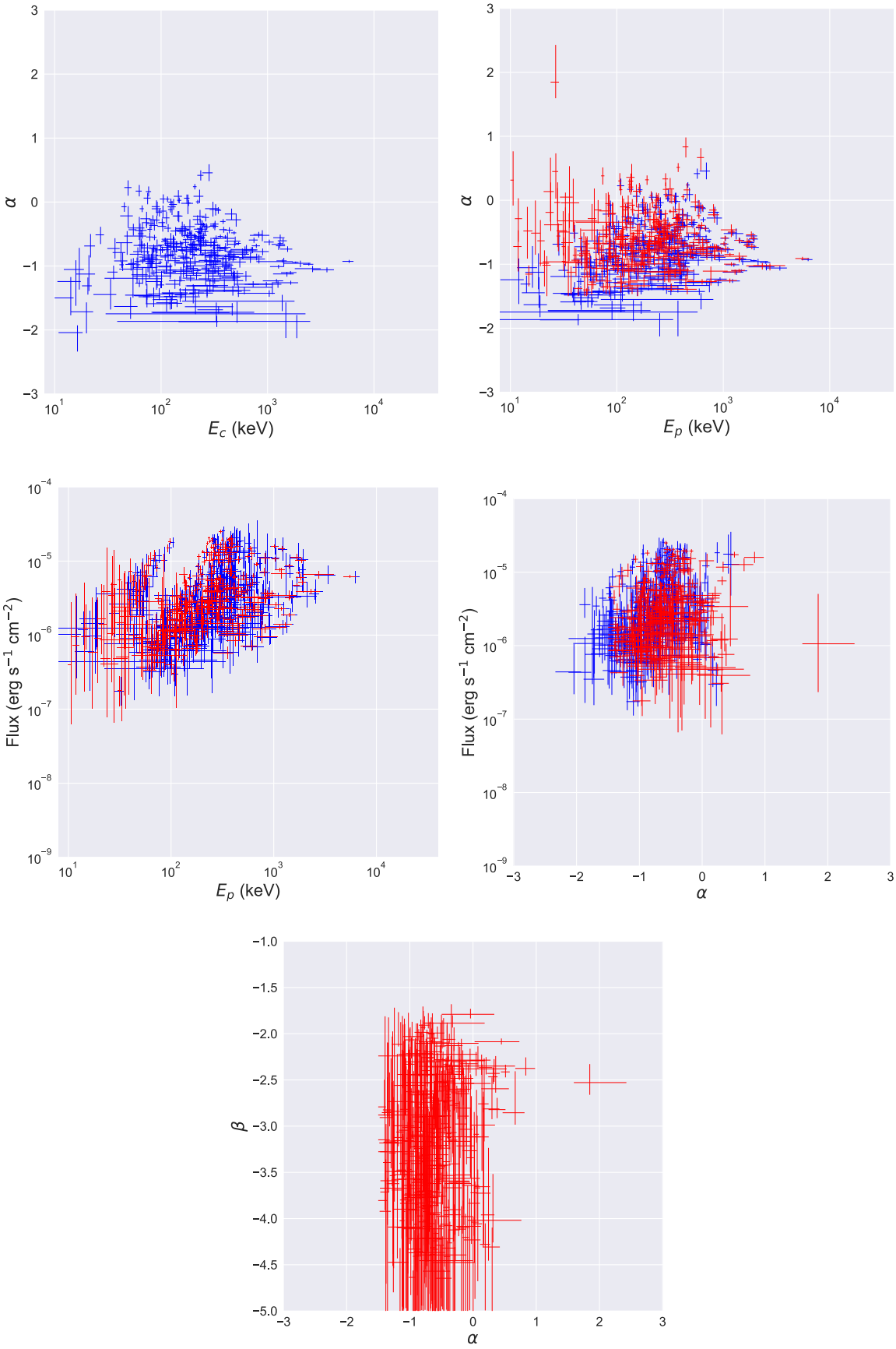

Figure 4. Global relations of the fitted parameters within the GBM energy range (8 keV–40 MeV) with statistical significance $S \geqslant 20$. Blue data points are for CPL and red for BAND.

3.5.3. F–α Relation

Finally, the F–α relations differ clearly from the two first relations, by it having a much more homogeneous behavior. In nearly all cases the relation is very similar, with a linear relation appearing in the semi-log plots. Of these, 32 pulses show a positive and 2 pulses show a negative relations (e.g., GRB 110920). In only three bursts there is nonmonotonic relation with a break, albeit being weak (GRBs 081009 [second episode], 110721, 160910). In the last case, GRB 090804, the relation is weak since there is only little variation in both the parameters. Again, this classification is shown in Table 1 by group 1 (34 pulses), group 2 (three pulses), and group 3 (one pulse), respectively.

To quantify the observed correlations, we again calculate the Spearman's rank coefficient (Table 1). Indeed, for a large majority of the pulses (28 cases) $r > 0.7$, and of these, 8 have very strong correlations, with values over 0.9. There are only two pulses which have weak correlations ($r < 0.4$).

We note that in the cases where the variation in $E_{\rm p}$ is small, it is only F and α that are correlated. An example is GRB 100528 for which the Golenetskii correlation is very weak, but the F–α is very clear.

The fact that the relation between F and α has a similar behavior for a majority of the pulses, instigates searches for possible functional relations between the parameters, for use in physical interpretations of the underlying mechanisms. With such an goal in mind, we have interpreted the F–α relation in the context of photospheric models in Ryde et al. (2019).

4. Summary and Conclusion

In summary, we have defined a sample of 38 single pulses from 37 GRBs out of 2050 *Fermi*/GBM detected bursts. These pulses all have more than 5 highly significant time bins, which allows time-resolved spectroscopy to be performed and the spectral evolution to be investigated. A total of 577 time-resolved spectra were obtained and their spectral properties investigated using a fully Bayesian method. The time bins were selected using the Bayesian block method (Scargle et al. 2013) in contrast to the signal-to-noise ratio method, employed in the previous time-resolved GRB spectral catalog (Yu et al. 2016). A new statistical measure of the data significance (Vianello 2018) was also used to indicate various significance levels.

We confirm the finding in previous catalogs that the cutoff power-law function is better than the Band function for most bursts, when considering the number of degrees of freedom. In the current study, we found that, among the frequently used empirical functions, a consistent description of the time-resolved spectra of GRB pulses could be achieved by using the power-law function with an exponential cutoff.

The distributions of the low-energy power-law slope and peak energy of the νF_ν spectra from the highest-significance time bins are consistent with previous results, while the distribution of the high-energy slope, when using a Band function instead of a cutoff power law, has a lower value than that of Yu et al. (2016). The latter study did not distinguish between single and composite pulses, which thus indicates that the high-energy slope observed in composite pulses might not be intrinsic in nature, but an effect of spectral evolution.

In contrast to previous catalogs, we also investigate the distribution of the maximal value of α in each pulse. Assuming that one and the same emission mechanism operates throughout the pulse, we show that the majority of the pulses (60%) are inconsistent with synchrotron emission, solely based on the line of death of $\alpha = -2/3$.

Finally, we found that a majority of the pulses have a congruent, monotonic behavior between the low-energy power-law index α and the energy flux F, which is largely independent of the flux variation in the light curve. This parameter correlation is studied in detail in a separate paper (Ryde et al. 2019).

We thank Damien Bégué J. Michael Burgess, Liang Li, Daniel Mortlock, and Asaf Pe'er for contributions in different parts of the project. We also thank the anonymous referee for the useful comments on the manuscript. This research made use of the High Energy Astrophysics Science Archive Research Center Online Service HEASARC at the NASA/Goddard Space Flight Center. We acknowledge support from the Swedish National Space Agency and the Swedish Research Council (Vetenskapsrådet). F.R. is supported by the Göran Gustafsson Foundation for Research in Natural Sciences and Medicine.

Facility: *Fermi*/GBM.

Software: `3ML` (Vianello et al. 2015).

Appendix A
Plots of the Evolutions

In Figure 5, we show the temporal evolutions of the inferred parameters for individual pulses.

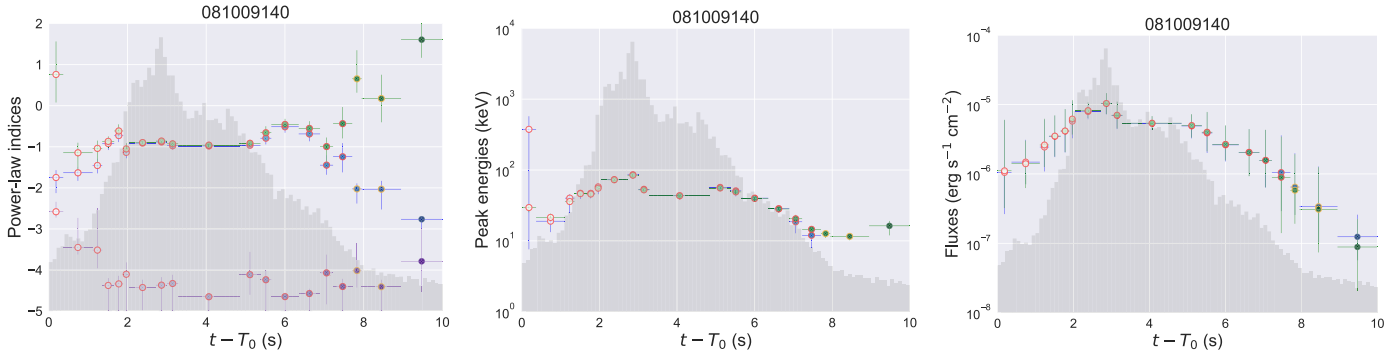

Figure 5. Left panel: temporal evolution of α (blue), $\alpha_{\rm BAND}$ (green), and $\beta_{\rm BAND}$ (purple). Middle panel: temporal evolution of $E_{\rm p}$ (blue) and $E_{\rm p,BAND}$ (green). Right panel: temporal evolution of F (blue) and $F_{\rm BAND}$ (green). Light curves are overlaid in gray color. Data points with red, orange, yellow, and no circles indicate statistical significance $S \geqslant 20$, $20 > S \geqslant 15$, $15 > S \geqslant 10$, and $S < 10$, respectively. Color scale from light blue (start) to deep blue (end) shows temporal evolution. Many of the low-significance data points are marginally or not constrained, as seen from the huge negative-side error bars.

(The complete figure set (38 images) is available.)

Appendix B
Plots of the correlations

In Figure 6, we show the correlations of the inferred parameters for individual pulses.

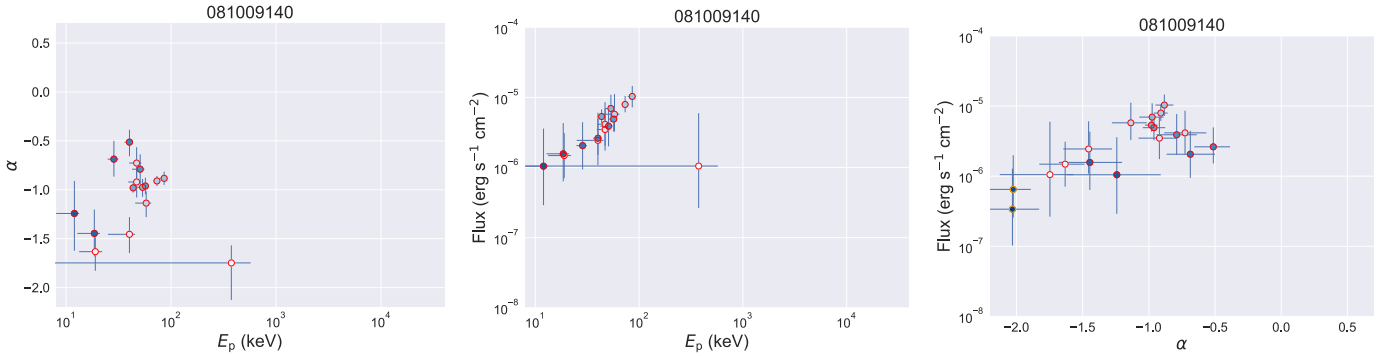

Figure 6. Left panel: relation of E_p–α. Middle panel: relation of F–E_p. Right panel: relation of F–α. Data points with red, orange, yellow, and no circles indicate statistical significance $S \geqslant 20$, $20 > S \geqslant 15$, $15 > S \geqslant 10$, and $S < 10$, respectively. Color scale from light blue (start) to deep blue (end) shows temporal evolution. Many of the low-significance data points are marginally or not constrained, as seen from the huge negative-side error bars. All the sources are available in the Figure Set.

(The complete figure set (38 images) is available.)

Appendix C
Table for All Results

In Table 3, we show all of the inferred parameters for individual pulses.

Table 3
Time-resolved Spectral Analysis Results of the First Pulse of GRB 081009140

t_{start} (1)	t_{stop} (2)	S (3)	K (4)	α (5)	E_c (6)	E_p (7)	F (8)	K_{BAND} (9)	α_{BAND} (10)	β_{BAND} (11)	$E_{p,BAND}$ (12)	F_{BAND} (13)	ΔDIC (14)	p_{DIC} (15)	$p_{DIC,BAND}$ (16)
0.00	0.37	21.26	$1.35^{+0.45}_{-1.15} \times 10^{+2}$	$-1.75^{+0.18}_{-0.38}$	$1485.52^{+786.01}_{-1455.41}$	$375.08^{+198.46}_{-367.47}$	$1.17^{+5.33}_{-0.87} \times 10^{-6}$	$4.78^{+1.48}_{-4.77} \times 10^{+1}$	$0.76^{+0.80}_{-0.68}$	$-2.58^{+0.24}_{-0.14}$	$29.55^{+2.61}_{-4.25}$	$9.83^{+104.80}_{-8.85} \times 10^{-7}$	−921.87	-125.85	-1030.44
0.37	1.11	47.27	$2.14^{+0.54}_{-1.04} \times 10^{+2}$	$-1.63^{+0.15}_{-0.20}$	$51.68^{+8.36}_{-15.47}$	$18.99^{+3.07}_{-5.68}$	$1.40^{+1.53}_{-0.69} \times 10^{-6}$	$5.55^{+0.59}_{-4.81} \times 10^{-1}$	$-1.15^{+0.25}_{-0.45}$	$-3.45^{+0.72}_{-0.17}$	$21.43^{+2.88}_{-1.85}$	$1.43^{+3.75}_{-1.08} \times 10^{-6}$	−236.43	-12.66	-242.95
1.11	1.36	39.67	$1.60^{+0.34}_{-0.94} \times 10^{+2}$	$-1.46^{+0.18}_{-0.19}$	$73.67^{+9.67}_{-27.70}$	$40.13^{+5.27}_{-15.09}$	$2.49^{+3.50}_{-1.37} \times 10^{-6}$	$7.73^{+2.00}_{-6.66} \times 10^{-1}$	$-1.04^{+0.19}_{-0.49}$	$-3.51^{+1.00}_{-0.44}$	$35.90^{+4.34}_{-3.65}$	$2.79^{+6.19}_{-2.00} \times 10^{-6}$	−212.93	-12.42	-220.78
1.36	1.66	57.40	$4.82^{+1.12}_{-2.20} \times 10^{+1}$	$-0.92^{+0.13}_{-0.16}$	$43.56^{+4.64}_{-7.33}$	$47.02^{+5.01}_{-7.91}$	$3.49^{+3.35}_{-1.80} \times 10^{-6}$	$7.49^{+1.21}_{-2.69} \times 10^{-1}$	$-0.87^{+0.12}_{-0.16}$	$-4.38^{+0.18}_{-0.62}$	$46.32^{+1.91}_{-2.19}$	$3.49^{+1.78}_{-1.17} \times 10^{-6}$	4.66	−6.30	1.16
1.66	1.89	58.50	$3.61^{+0.82}_{-1.81} \times 10^{+1}$	$-0.73^{+0.16}_{-0.16}$	$36.90^{+3.91}_{-5.64}$	$46.98^{+4.98}_{-7.18}$	$4.30^{+4.30}_{-2.28} \times 10^{-6}$	$1.58^{+0.27}_{-0.72} \times 10^{+0}$	$-0.61^{+0.16}_{-0.18}$	$-4.34^{+0.20}_{-0.66}$	$45.78^{+1.72}_{-2.10}$	$4.20^{+2.67}_{-1.57} \times 10^{-6}$	5.61	−8.96	-1.60
1.89	2.04	58.07	$1.18^{+0.26}_{-0.51} \times 10^{+2}$	$-1.14^{+0.12}_{-0.14}$	$67.09^{+7.75}_{-14.36}$	$57.95^{+6.69}_{-12.40}$	$6.06^{+5.55}_{-2.76} \times 10^{-6}$	$7.44^{+1.06}_{-2.88} \times 10^{-1}$	$-1.05^{+0.14}_{-0.16}$	$-4.10^{+0.29}_{-0.89}$	$55.36^{+3.00}_{-3.72}$	$6.12^{+3.20}_{-2.23} \times 10^{-6}$	0.58	−4.09	-0.11
2.04	2.72	140.80	$5.96^{+0.75}_{-0.96} \times 10^{+1}$	$-0.91^{+0.05}_{-0.05}$	$67.28^{+3.93}_{-4.50}$	$73.36^{+4.28}_{-4.90}$	$8.06^{+2.44}_{-1.72} \times 10^{-6}$	$9.21^{+0.81}_{-0.98} \times 10^{-1}$	$-0.90^{+0.05}_{-0.05}$	$-4.43^{+0.19}_{-0.55}$	$72.69^{+1.77}_{-1.87}$	$8.19^{+1.28}_{-1.01} \times 10^{-6}$	−2.09	1.96	3.26
2.72	3.00	102.35	$5.87^{+0.93}_{-1.32} \times 10^{+1}$	$-0.88^{+0.07}_{-0.07}$	$76.95^{+5.66}_{-7.33}$	$85.94^{+6.32}_{-8.19}$	$1.01^{+0.45}_{-0.31} \times 10^{-5}$	$1.04^{+0.11}_{-0.16} \times 10^{+0}$	$-0.86^{+0.07}_{-0.08}$	$-4.37^{+0.20}_{-0.63}$	$84.43^{+2.85}_{-3.59}$	$1.05^{+0.23}_{-0.17} \times 10^{-5}$	−0.25	1.28	3.00
3.00	3.29	91.89	$9.24^{+1.64}_{-2.72} \times 10^{+1}$	$-0.98^{+0.09}_{-0.10}$	$52.22^{+4.26}_{-5.97}$	$53.52^{+4.36}_{-6.11}$	$6.73^{+4.00}_{-2.33} \times 10^{-6}$	$1.13^{+0.15}_{-0.27} \times 10^{+0}$	$-0.93^{+0.09}_{-0.10}$	$-4.33^{+0.21}_{-0.67}$	$52.48^{+1.75}_{-1.96}$	$7.06^{+2.10}_{-1.70} \times 10^{-6}$	−0.22	-0.24	2.45
3.29	4.84	181.02	$8.87^{+0.94}_{-1.23} \times 10^{+1}$	$-0.98^{+0.05}_{-0.05}$	$42.72^{+1.86}_{-2.14}$	$43.54^{+1.89}_{-2.18}$	$5.32^{+1.33}_{-1.01} \times 10^{-6}$	$1.02^{+0.09}_{-0.12} \times 10^{+0}$	$-0.96^{+0.05}_{-0.05}$	$-4.65^{+0.09}_{-0.35}$	$43.23^{+0.74}_{-0.67}$	$5.40^{+0.98}_{-0.76} \times 10^{-6}$	0.44	2.06	2.95
4.84	5.38	93.03	$5.77^{+0.98}_{-1.55} \times 10^{+1}$	$-0.96^{+0.08}_{-0.08}$	$54.84^{+4.14}_{-5.96}$	$56.95^{+4.30}_{-6.19}$	$4.85^{+2.37}_{-1.56} \times 10^{-6}$	$7.54^{+0.96}_{-1.59} \times 10^{-1}$	$-0.91^{+0.08}_{-0.09}$	$-4.11^{+0.55}_{-0.49}$	$55.71^{+1.79}_{-1.86}$	$4.92^{+1.46}_{-1.02} \times 10^{-6}$	−1.90	-0.04	2.73
5.38	5.65	58.32	$3.50^{+0.72}_{-1.73} \times 10^{+1}$	$-0.79^{+0.15}_{-0.15}$	$41.98^{+4.19}_{-6.92}$	$50.80^{+5.07}_{-8.38}$	$3.97^{+3.64}_{-2.05} \times 10^{-6}$	$1.20^{+0.19}_{-0.53} \times 10^{+0}$	$-0.66^{+0.16}_{-0.18}$	$-4.24^{+0.24}_{-0.76}$	$49.09^{+2.10}_{-2.14}$	$3.88^{+2.18}_{-1.47} \times 10^{-6}$	3.14	−7.04	-1.53
5.65	6.35	75.49	$1.68^{+0.37}_{-0.70} \times 10^{+1}$	$-0.51^{+0.13}_{-0.14}$	$27.01^{+2.07}_{-2.79}$	$40.16^{+3.08}_{-4.15}$	$2.56^{+2.03}_{-1.10} \times 10^{-6}$	$1.76^{+0.31}_{-0.64} \times 10^{+0}$	$-0.46^{+0.14}_{-0.14}$	$-4.65^{+0.09}_{-0.35}$	$39.63^{+1.08}_{-1.01}$	$2.66^{+1.46}_{-0.93} \times 10^{-6}$	8.07	−8.16	-0.82
6.35	6.89	57.49	$3.42^{+0.77}_{-1.81} \times 10^{+1}$	$-0.69^{+0.19}_{-0.18}$	$21.74^{+2.21}_{-2.78}$	$28.55^{+2.90}_{-3.65}$	$1.92^{+2.27}_{-1.02} \times 10^{-6}$	$2.03^{+0.35}_{-1.16} \times 10^{+0}$	$-0.55^{+0.18}_{-0.23}$	$-4.57^{+0.12}_{-0.43}$	$28.22^{+1.34}_{-1.06}$	$2.10^{+2.03}_{-1.05} \times 10^{-6}$	1.07	−13.85	-13.43
6.89	7.22	38.60	$2.12^{+0.39}_{-1.45} \times 10^{+2}$	$-1.45^{+0.24}_{-0.23}$	$33.53^{+4.42}_{-10.41}$	$18.58^{+2.45}_{-5.77}$	$1.70^{+2.94}_{-1.02} \times 10^{-6}$	$1.11^{+0.16}_{-0.96} \times 10^{+0}$	$-0.99^{+0.22}_{-0.45}$	$-4.07^{+0.44}_{-0.77}$	$20.50^{+2.78}_{-2.13}$	$1.63^{+3.84}_{-1.18} \times 10^{-6}$	−129.60	-24.08	-149.93
7.22	7.71	31.50	$1.84^{+0.31}_{-1.51} \times 10^{+2}$	$-1.24^{+0.33}_{-0.38}$	$15.83^{+1.77}_{-5.22}$	$12.00^{+1.34}_{-3.95}$	$9.38^{+24.68}_{-6.49} \times 10^{-7}$	$6.45^{+0.27}_{-5.95} \times 10^{+0}$	$-0.44^{+0.40}_{-0.36}$	$-4.40^{+0.19}_{-0.60}$	$14.57^{+1.40}_{-1.42}$	$1.07^{+3.98}_{-0.85} \times 10^{-6}$	−83.98	-65.80	-146.92
7.71	7.95	15.08	$6.11^{+3.88}_{-1.32} \times 10^{+2}$	$-2.02^{+0.13}_{-0.36}$	$36.51^{+3.66}_{-24.80}$	$-0.90^{+0.09}_{-0.61}$	$6.17^{+12.35}_{-3.80} \times 10^{-7}$	$2.41^{+0.26}_{-2.39} \times 10^{+2}$	$0.65^{+0.70}_{-0.34}$	$-4.01^{+0.66}_{-0.41}$	$12.68^{+1.19}_{-1.66}$	$6.96^{+65.80}_{-6.29} \times 10^{-7}$	−122.81	-32.70	-152.33
7.95	8.95	15.27	$4.70^{+1.57}_{-3.90} \times 10^{+2}$	$-2.03^{+0.20}_{-0.49}$	$19.81^{+1.29}_{-9.81}$	$-0.61^{+0.04}_{-0.30}$	$3.22^{+9.24}_{-2.25} \times 10^{-7}$	$5.17^{+0.94}_{-5.15} \times 10^{+1}$	$0.18^{+0.58}_{-0.58}$	$-4.41^{+0.17}_{-0.59}$	$11.59^{+0.59}_{-1.38}$	$2.92^{+36.42}_{-2.68} \times 10^{-7}$	−672.65	-34.82	-707.46
8.95	10.00	5.45	$3.36^{+1.38}_{-1.93} \times 10^{+2}$	$-2.76^{+0.06}_{-0.24}$	$4946.77^{+1892.03}_{-4908.87}$	$-3771.55^{+1442.54}_{-3742.65}$	$1.21^{+1.48}_{-0.68} \times 10^{-7}$	$2.94^{+0.88}_{-2.94} \times 10^{+2}$	$1.61^{+0.81}_{-0.44}$	$-3.79^{+0.79}_{-0.74}$	$16.30^{+2.83}_{-4.33}$	$8.36^{+99.21}_{-7.87} \times 10^{-8}$	−70.97	0.73	−70.73

Note. Time-resolved spectral analysis results of the first pulse of GRB 081009140. Columns (1) and (2) list the start and stop times (in units of s) of the Bayesian block time bins. Column (3) lists the significance of the bin. Columns (4)–(6) list the best-fit parameters for the CPL model. Column (7) lists the derived values of E_p for the CPL model. Column (8) lists the derived CPL energy flux. Columns (9)–(12) list the best-fit parameters for the BAND model. Column (13) lists the derived BAND energy flux. Column (14) lists the difference between the Deviance Information Criterion (DIC) for the CPL and BAND model, $\Delta DIC = DIC_{BAND} - DIC_{CPL}$. Columns (15) and (16) list the effective number of parameters for the CPL and BAND model, respectively. All time parameters have units of s, normalizations have units of ph s^{-1} cm^{-2} keV^{-1}, energies have units of keV, and fluxes have units of erg s^{-1} cm^{-2}. N/A means that a reliable value of the flux could not be computed due to large errors in the fitted parameters. The full version contains all of the spectral analysis results for all GRBs.

(This table is available in its entirety in machine-readable form.)

ORCID iDs

Hoi-Fung Yu https://orcid.org/0000-0001-5643-7445
Hüsne Dereli-Bégué https://orcid.org/0000-0002-8852-7530
Felix Ryde https://orcid.org/0000-0002-9769-8016

References

Abdo, A. A., Ackermann, M., Ajello, M., et al. 2009, ApJL, 706, L138
Ackermann, M., Ajello, M., Baldini, L., et al. 2010, ApJL, 717, L127
Axelsson, M., Baldini, L., Barbiellini, G., et al. 2012, ApJL, 757, L31
Band, D., Matteson, J., Ford, L., et al. 1993, ApJ, 413, 281
Barat, C., Lestrade, J. P., Dezalay, J.-P., et al. 2000, ApJ, 538, 152
Basak, R., & Rao, A. R. 2014, MNRAS, 442, 419
Bissaldi, E., von Kienlin, A., Lichti, G., et al. 2009, ExA, 24, 47
Borgonovo, L. 2001, ApJ, 548, 770
Burgess, J. M. 2014, MNRAS, 445, 2589
Burgess, J. M., Preece, R. D., Ryde, F., et al. 2014, ApJL, 784, L43
Cash, W. 1979, ApJ, 228, 939
Connaughton, V., Briggs, M. S., Goldstein, A., et al. 2015, ApJS, 216, 32
Crider, A., Liang, E. P., Smith, I. A., et al. 1997, ApJL, 479, L39
Firmani, C., Cabrera, J. I., Avila-Reese, V., et al. 2009, MNRAS, 393, 1209
Gelman, A., Hwang, J., & Vehtari, A. 2014, Statistics and Computing, 24, 6
Ghirlanda, G., Celotti, A., & Ghisellini, G. 2002, A&A, 393, 409
Ghirlanda, G., Celotti, A., & Ghisellini, G. 2003, A&A, 406, 879
Ghirlanda, G., Nava, L., & Ghisellini, G. 2010, A&A, 511, 43
Goldstein, A., Burgess, J. M., Preece, R. D., et al. 2012, ApJS, 199, 19
Golenetskii, S. V., Mazets, E. P., Aptekar, R. L., & Ilinskii, V. N. 1983, Natur, 306, 451
González, M. M., Dingus, B. L., Kaneko, Y., et al. 2003, Natur, 424, 749
Greiner, J., Burgess, J. M., Savchenko, V., & Yu, H.-F. 2016, ApJL, 827, L38
Gruber, D., Goldstein, A., Weller von Ahlefeld, V., et al. 2014, ApJS, 211, 12
Guiriec, S., Briggs, M. S., Connaugthon, V., et al. 2010, ApJ, 725, 225
Guiriec, S., Connaughton, V., Briggs, M. S., et al. 2011, ApJL, 727, L33
Guiriec, S., Daigne, F., Hascoët, R., et al. 2013, ApJ, 770, 32
Guiriec, S., Gonzalez, M. M., Sacahui, J. R., et al. 2016a, ApJ, 819, 79
Guiriec, S., Kouveliotou, C., Daigne, F., et al. 2015a, ApJ, 807, 148
Guiriec, S., Kouveliotou, C., Hartmann, D. H., et al. 2016b, ApJL, 831, L8
Guiriec, S., Mochkovitch, R., Piran, T., et al. 2015b, ApJ, 814, 10
Hakkila, J., & Giblin, T. W. 2006, ApJ, 646, 1086
Kaneko, Y., Preece, R. D., Briggs, M. S., et al. 2006, ApJS, 166, 298
Lazzati, D., Morsony, B. J., Margutti, R., & Begelman, M. C. 2013, ApJ, 765, 103
Lloyd, N. M., & Petrosian, V. 2000, ApJ, 543, 722
Lloyd-Ronning, N. M., & Petrosian, V. 2002, ApJ, 565, 182
Lu, R.-J., Wei, J.-J., Liang, E.-W., et al. 2012, ApJ, 756, 112
Meegan, C., Lichti, G., Bhat, P. N., et al. 2009, ApJ, 702, 791
Nappo, F., Pescalli, A., Oganesyan, G., et al. 2017, A&A, 598, A23
Norris, J. P., Nemiroff, R. J., Bonnell, J. T., et al. 1996, ApJ, 459, 393
Norris, J. P., Share, G. H., Messina, D. C., et al. 1986, ApJ, 301, 213
Oganesyan, G., Nava, L., Ghirlanda, G., & Celotti, A. 2018, A&A, 616, A138
Preece, R., Briggs, M. S., Mallozzi, R. S., et al. 1998, ApJ, 506, 23
Ryde, F. 2004, ApJ, 614, 827
Ryde, F. 2005, ApJ, 625, 95
Ryde, F., Axelsson, M., Zhang, B. B., et al. 2010, ApJL, 709, L172
Ryde, F., Pe'er, A., Nymark, T., et al. 2011, MNRAS, 415, 3693
Ryde, F., & Svensson, R. 1999, ApJ, 512, 693
Ryde, F., Yu, H.-F., Dereli-Bégué, H., et al. 2019, MNRAS, 484, 1912
Scargle, J. D., Norris, J. P., Jackson, B., & Chiang, J. 2013, arXiv:1304.2818
Spiegelhalter, D. J., Best, N. G., Carlin, B. P., & van der Linde, A. 2002, J. R. Statist. Soc. B, 64, 583
Vianello, G. 2018, ApJS, 236, 17
Vianello, G., Gill, R., Granot, J., et al. 2018, ApJ, 864, 163
Vianello, G., Lauer, R. J., Younk, P., et al. 2015, arXiv:1507.08343
Yu, H.-F., Preece, R. D., Greiner, J., et al. 2016, A&A, 588, A135
Zhang, B.-B., Uhm, Z. L., Connaughton, V., Briggs, M. S., & Zhang, B. 2016, ApJ, 816, 72
Zhang, B.-B., Zhang, B., Castro-Tirado, A. J., et al. 2018, NatAs, 2, 69